Interior Water-Mass Variability in the Southern Hemisphere Oceans during the Last Decade

Esther Portela, Nicolas Kolodziejczyk, Christophe Maes, Virginie Thierry

Interior Water-Mass Variability in the Southern Hemisphere Oceans during the Last Decade

ESTHER PORTELA, NICOLAS KOLODZIEJCZYK, CHRISTOPHE MAES, AND VIRGINIE THIERRY

Univ. Brest, Laboratoire d'Océanographie Physique et Spatiale, CNRS, IRD, Ifremer, Plouzané, France

(Manuscript received 28 May 2019, in final form 15 November 2019)

ABSTRACT

Using an Argo dataset and the ECCOv4 reanalysis, a volume budget was performed to address the main mechanisms driving the volume change of the interior water masses in the Southern Hemisphere oceans between 2006 and 2015. The subduction rates and the isopycnal and diapycnal water-mass transformation were estimated in a density–spiciness (σ–τ) framework. Spiciness, defined as thermohaline variations along isopycnals, was added to the potential density coordinates to discriminate between water masses spreading on isopycnal layers. The main positive volume trends were found to be associated with the Subantarctic Mode Waters (SAMW) in the South Pacific and South Indian Ocean basins, revealing a lightening of the upper waters in the Southern Hemisphere. The SAMW exhibits a two-layer density structure in which subduction and diapycnal transformation from the lower to the upper layers accounted for most of the upper-layer volume gain and lower-layer volume loss, respectively. The Antarctic Intermediate Waters, defined here between the 27.2 and 27.5 kg m^{-3} isopycnals, showed the strongest negative volume trends. This volume loss can be explained by their negative isopyncal transformation southward of the Antarctic Circumpolar Current into the fresher and colder Antarctic Winter Waters (AAWW) and northward into spicier tropical/subtropical Intermediate Waters. The AAWW is destroyed by obduction back into the mixed layer so that its net volume change remains nearly zero. The proposed mechanisms to explain the transformation within the Intermediate Waters are discussed in the context of Southern Ocean dynamics. The σ–τ decomposition provided new insight on the spatial and temporal water-mass variability and driving mechanisms over the last decade.

1. Introduction

The ocean water-mass variability is intimately linked to the atmospheric changes as they are imprinted at the ocean surface by the natural climate modulation and anthropogenic forcing. Recent studies have shown that the ocean warming during the last decade has been mainly concentrated in the extratropical Southern Hemisphere (Häkkinen et al. 2016; Roemmich et al. 2015; Kolodziejczyk et al. 2019). In particular, hot spots of ocean warming have been localized in the southern Pacific and Indian Oceans with the largest decadal ocean heat content (OHC) trend being mainly associated with the Subtropical and Subantarctic Mode Waters (SAMW) (Gao et al. 2018; Häkkinen et al. 2016; Desbruyères et al. 2017; Kolodziejczyk et al. 2019). At interannual to decadal time scales, wind-driven isopycnal heaving (Häkkinen et al. 2016) drives the OHC variability while the isopycnal increase of temperature (spiciness) has a minor contribution, with the exception of regions of intense vertical mixing in the North Atlantic and Southern Oceans (Desbruyères et al. 2017; Häkkinen et al. 2016). The existing studies suggest that mode waters, by their ability to store heat, play a key role in the climate regulation (Gao et al. 2018). However, no driver or mechanism has been clearly identified to explain decadal variability in the water masses of the Southern Hemisphere oceans (SHOs).

The water masses of the Southern Ocean play an important role in the global climate system and circulation (Marshall and Speer 2012; Naveira Garabato et al. 2009; Rintoul 2018). It is dynamically dominated by the wind-driven Antarctic Circumpolar Current (ACC), the largest current of the global ocean in terms of volume transport [173.3 Sv (1 Sv $\equiv 10^6$ m^3 s^{-1}); Donohue et al. 2016], which connects all of the ocean basins.

Supplemental information related to this paper is available at the Journals Online website: https://doi.org/10.1175/JPO-D-19-0128.s1.

Corresponding author: Esther Portela, eportelah@gmail.com

DOI: 10.1175/JPO-D-19-0128.1

The geostrophic balance of the strong eastward flow of the ACC results in strongly tilted isopycnals rising to the south (Böning et al. 2008) that represent an adiabatic pathway for the upwelling of Circumpolar Deep Water (CDW) to the surface. The release of potential energy stored in the sloping isopycnals by baroclinic instability generates the eddy field associated with the ACC. This meridional eddy flux plays a central role in the dynamics and thermodynamics of the Southern Ocean (Nowlin and Klinck 1986); it compensates the wind-driven northward Ekman transport with an opposed mass transport to the south that acts to flatten the isopycnals with the result being the so-called "eddy compensation" (Marshall and Radko 2003; Marshall and Speer 2012). This balance between the eddy field and the mean ACC flow forms the residual overturning circulation (Marshall and Radko 2003; Marshall and Speer 2012; Rintoul and Naveira Garabato 2013), which is of key importance in the advection of tracers and properties in the Southern Ocean (Marshall and Speer 2012). Although the overturning circulation is mainly an adiabatic process in the ocean interior, diapycnal mixing also plays a significant role by driving water-mass transformations that are important to the global overturning. This diapycnal mixing is dominant in the mixed layer and near the bottom (Rintoul and Naveira Garabato 2013), the latter, due to the interaction with the topography (Mashayek et al. 2017). In contrast, in the interior ocean diapycnal mixing is weak (Rintoul 2018) in comparison with mixing along isopycnals.

When the CDW gets to the surface along the tilted isopycnals in the Southern Ocean, it takes two different paths. The densest (hereinafter Lower) (L)CDW outcrops near Antarctica where it is transformed by cooling and brine rejection into the denser Antarctic Bottom Water (AABW) (Rintoul and Naveira Garabato 2013; Abernathey et al. 2016; Tamsitt et al. 2018). This process constitutes the lower branch of the Southern Ocean Overturning Circulation. The less dense (hereinafter Upper) (U)CDW outcrops within the ACC belt where it is transformed, by means of warming and freshening, into the lighter Antarctic Intermediate Waters (AAIW) and SAMW. Both, AAIW and SAMW are then transported northward and subducted into the pycnocline (Hanawa and Talley 2001) during winter buoyancy loss in the mixed layer (McCartney and Talley 1982; McCartney 1977). This water formation and subduction constitute the upper branch of the Southern Ocean Overturning Circulation (Abernathey et al. 2016; Sloyan and Rintoul 2001; Zika et al. 2009).

The SAMW comprises different modes due to the zonal variation of its properties in relation to the meridional shift of the Subantarctic Front around the Southern Ocean (Hanawa and Talley 2001). The densest, and least spicy (coldest and freshest) SAMW is found in the eastern South Pacific around the Drake Passage and it becomes lighter and spicier (warmer and saltier) westward of this location. The lightest mode of the SAMW lies on the $26.5\,\mathrm{kg\,m^{-3}}$ isopycnal in the eastern South Atlantic and western South Indian basins.

Denser than the SAMW, the AAIW is characterized by a relative salinity minimum located around 800–1000 m depth. AAIW is found near the surface south of the Polar Front and then deepens until around 1000 m depth as it moves northward in midlatitudes (Piola and Georgi 1982). So far, there is no agreement in the literature about the formation of AAIW. Some authors have proposed that it forms by subduction of the densest type of SAMW in the eastern Pacific (Hanawa and Talley 2001; Piola and Georgi 1982). However, in this region, the similarity of properties between these two water masses also suggests that the AAIW salinity minimum could be formed by convective overturning (McCartney 1977). In contrast with these theories, Naveira Garabato et al. (2009) attribute the formation of AAIW in the Drake Passage to the annual frontal mesoscale subduction of a colder and fresher variety of Intermediate Waters, the Antarctic Winter Water (AAWW).

AAWW extends northward from the Antarctic continent within the first 200 m of the water column and it is subjected to strong seasonal changes: relatively thick layers of AAWW are found in winter but they erode in late summer, when surface waters warm through diapycnal mixing (Evans et al. 2014). At time scales from subannual to interannual, the variability of AAWW is intimately linked to that of the AAIW (Naveira Garabato et al. 2009). Despite the recent efforts in the description and understanding of the AAWW properties and driving dynamics, there is still little knowledge of its variability and the role it plays in the modulation of the AAIW properties at interannual to decadal time scales. From now on, we will use the general term Intermediate Waters (IW) to refer to the AAIW and AAWW together and any other water mass in the SHOs within the same density range.

Based on the method first introduced by Walin (1982) to compute water-mass transformation in thermohaline coordinates, we used a density–spice (σ–τ) framework to investigate the decadal volume trend of interior water masses in the SHOs by means of a volume budget. Potential density is the natural coordinate to separate isopycnal (diaspice) and diapycnal mass fluxes while spiciness, defined as the thermohaline variations along isopycnals (following the definition of McDougall and Krzysik 2015), is added as a second dimension in the

volume budget. Spiciness is a meaningful variable to identify different water masses spreading along isopycnals (Jackett and McDougall 1985; McDougall and Krzysik 2015). This approach allows the identification of finer-scale and local features in comparison to previous studies performing water-mass transformation in density coordinates only (Badin et al. 2013; Abernathey et al. 2016; Nurser et al. 1999; Downes et al. 2011; Speer et al. 2000).

Most of the studies have addressed the mean or seasonal water-mass transformation by means of buoyancy fluxes in the mixed layer (Abernathey et al. 2016; Evans et al. 2014; Nurser et al. 1999; Badin et al. 2013). While the mixed layer waters are subject to seasonal modifications, at longer time scales these surface conditions are partially retained in the ocean interior by subduction during late winter (Luyten et al. 1983; Marshall et al. 1999; Stommel 1979). In this study we address the spatial and temporal variability of the SAMW and IW in the SHOs during the last decade. Using an Argo dataset and outputs from the ECCOv4 reanalysis to diagnose the mass flux between the water masses, we computed the average interior water-mass transformation. The volume budget is closed by using the subduction rate through the deepest mixed layer over the period 2006–15.

2. Methods

a. Data and processing

This study is based on the monthly gridded fields of Conservative Temperature Θ and Absolute Salinity S_A obtained from the In Situ Analysis System (ISAS), an optimal interpolated product of the Argo global dataset (Gaillard et al. 2016), between 2006 and 2015. Over those 10 years, the global coverage of the Argo profiles has enough temporal and spatial resolution to explore the water-mass variability in the SHOs. The temperature and salinity fields are reconstructed on 152 depth levels ranging from 0 to 2000 m and then converted to Θ and S_A (McDougall and Barker 2011). From these hydrographic data we computed the geostrophic velocity field relative to 1000 m that was used to assess the lateral induction term of subduction. The mean reference velocity at that depth level, was obtained from ''ANDRO,'' an Argo-based deep displacement dataset (Ollitrault and Rannou 2013; Ollitrault and Colin de Verdière 2014).

In addition we used monthly geostrophic and bolus velocity estimates obtained from the ''Estimating the Circulation and Climate of the Ocean version 4 state estimate'' (ECCOv4, http://www.ecco-group.org; Forget et al. 2015) to compute the eddy-induced subduction. The estimate describes the full-depth, three-dimensional, time-evolving oceanic state, and it is a solution to an ocean general circulation model, constrained with most available ocean data.

Spiciness (τ; kg m^{-3}) was computed from Θ and S_A fields following the International Thermodynamic Equation of Seawater—2010 (TEOS-10) routines (McDougall and Barker 2011). The Θ and S_A isolines displayed in the σ–τ diagram were computed from σ and τ values with a routine adapted from the TEOS-10 functions (provided by Dr. T. McDougall).

The volume integration was made in σ–τ classes with density intervals of 0.1 kg m^{-3} between 25 and 27.5 kg m^{-3} and spiciness intervals of 0.2 kg m^{-3} between -0.6 and 3 kg m^{-3}. This choice results from a trade-off between the representation of each class and the accuracy in the water-mass identification. Within the Southern Ocean, the waters denser than 27.5 kg m^{-3} are not systematically resolved by the 2000-m-depth Argo network and therefore they are not considered in this study.

The MLD was computed from the interpolated density field using a density criterion of $\Delta\sigma = 0.03$ kg m^{-3} (de Boyer Montégut et al. 2004; Dong et al. 2008); and then spatially smoothed with a running mean filter. The aim of the smoothing was to reduce the noise associated to the horizontal gradient of the MLD necessary to compute the lateral induction contribution to subduction. Several tests on MLD computation were performed using different criteria, mapping methods and smoothing to obtain the better trade-off between the preservation of an accurate MLD structure and the estimation of a reliable subduction rate. For example, smoothing methods that propagate the land mask and those that greatly reduced the maximum depth of the mixed layer, as convolution or Gaussian filters, were discarded. Preliminary tests showed that the subduction magnitude decreases exponentially as a function of the smoothing scale and converges to an asymptotic value (Fig. S2 and explanation in the online supplemental material). Following this result and other criteria detailed in the online supplemental material (i.e., comparison between ISAS and ECCOv4 at different smoothing scales; online supplemental Fig. S1), the moving mean window of the running mean was set to 10°. Even with this important smoothing, the magnitude of the resulting subduction was greater than that reported by Sallée et al. (2010) using the same computation method, which suggests that different gridding or smoothing processes were applied in both studies. Our results were more similar in magnitude and in the spatial scale of the subduction structures to others obtained

from models in the same region (Langlais et al. 2017; Downes et al. 2017).

The volume trends were computed for every σ–τ class by linear fitting considering significance at 95%. The trend fits with a r^2 value lower than an ad hoc value estimated to be 0.2 were discarded to prevent from aliasing of the rend with higher frequency interannual variability. Of the total number of σ–τ classes with any representation in volume, 50% showed significant trends, but only 18% were significant and had r^2 values higher than 0.2.

b. Density–spiciness framework

The analyses carried out in this study were performed in σ–τ coordinates. This choice was made for different reasons. 1) Potential density is the natural coordinate to study the ocean dynamics, and it provides information about the isopycnal and diapycnal nature of the mechanisms driving the volume change. 2) Spiciness variations reflect the thermohaline changes in density units (McDougall and Krzysik 2015; Jackett and McDougall 1985). Those changes are a proxy for the contrast between water masses spreading along isopycnals that are missed by using density coordinates only. Following McDougall and Krzysik (2015) spiciness is assumed to be proportional to isopycnal temperature and salinity while the suggested orthogonality between density and spiciness isolines (Flament 2002; Huang 2011) is devoid of physical meaning and is not assumed in our spiciness definition.

3. Volume budget

Based on Argo data, we performed a complete volume budget in σ–τ coordinates for the interior ocean. The water-mass volume change dV/dt between 2006 and 2015 was addressed as a combination of 1) subduction S through the base of the deepest MLD over the 10-yr period, 2) water-mass formation $\sum U_{(\sigma,\tau)}$ (convergence or divergence of the interior fluxes), and 3) the exchange flux across the domain's geographical limits Ψ.

The volume budget can be expressed as

$$\underbrace{dV/dt}_{\text{10-yr trend}} = \underbrace{S}_{\text{Subduction}} + \underbrace{\sum U}_{\text{Formation}} + \underbrace{\Psi}_{\text{Exchange flux}}, \quad (1)$$

where subduction is the mass flux between the mixed layer and the interior waters at a given σ–τ class, if this is in contact with the base of the deepest mixed layer. Here, U is the water-mass transformation due to isopycnal/diapycnal mixing fluxes, whereas its convergence or divergence represented by the sum ($\sum$) of the interior fluxes across the geographical limits of a given σ–τ class represents water-mass formation or destruction, respectively (Donners et al. 2005; Walin 1982). Finally, Ψ is the exchange flux across the domain limits: the equator to the north and 70°S to the south. Because we are only considering the interior waters, the buoyancy flux is not taken into account, instead, the imprinting of the atmosphere into the ocean is accounted for by diagnosing subduction, which connects the mixed layer with the ocean interior. Consequently, the water-mass transformation term excludes the exchanges between the MLD and interior waters.

A sketch of how the change in the water characteristics is represented in the σ–τ diagrams is shown in Fig. 1a, and all the important processes involved in the volume change of a σ–τ class are represented in geographical coordinates in Fig. 1b. A single σ–τ class (square) in Fig. 1a is gray-shaded in Fig. 1b. It is shown that a σ–τ class can increase volume 1) by convergence of interior fluxes (formation) across the σ or τ limits, 2) by subduction of water across the base of the mixed layer without crossing any σ–τ class limits, or 3) by an exchange flux of water within a given σ–τ class across the domain's limits. Subduction/obduction and exchange flux occur without an associated water-mass transformation.

a. Subduction

The subduction rate was computed as the flux across the time-fixed surface (Marshall et al. 1993; Price 2001) defined by the deepest MLD over the period 2006–15. The MLD varies seasonally with the consequent entrainment and detrainment of water into the mixed layer and the interior ocean respectively. Subduction refers to the fraction of water that has entered into the thermocline and does not return to the MLD (Donners et al. 2005). This approach ensures that subduction involves an actual physical transfer of fluid year-round between the mixed layer and the ocean interior. Equation (2) details the three main components of the total mean subduction rate:

$$\underbrace{S(x,y)}_{\text{Subduction}} = \underbrace{u_h \cdot \nabla_h H}_{\text{Lateral induction}} + \underbrace{w_H}_{\substack{\text{Vertical}\\ \text{velocity}}} + \underbrace{\nabla_h (u_h^* H)}_{\text{Eddy induced}}, \quad (2)$$

Subduction is positive downward. The lateral induction term is given by the horizontal geostrophic velocity u_h and the horizontal gradient of the deepest MLD H.

Following Marshall et al. (1993), the vertical velocity term w_H can be estimated as formed by the Ekman pumping and the vertical geostrophic velocity by using

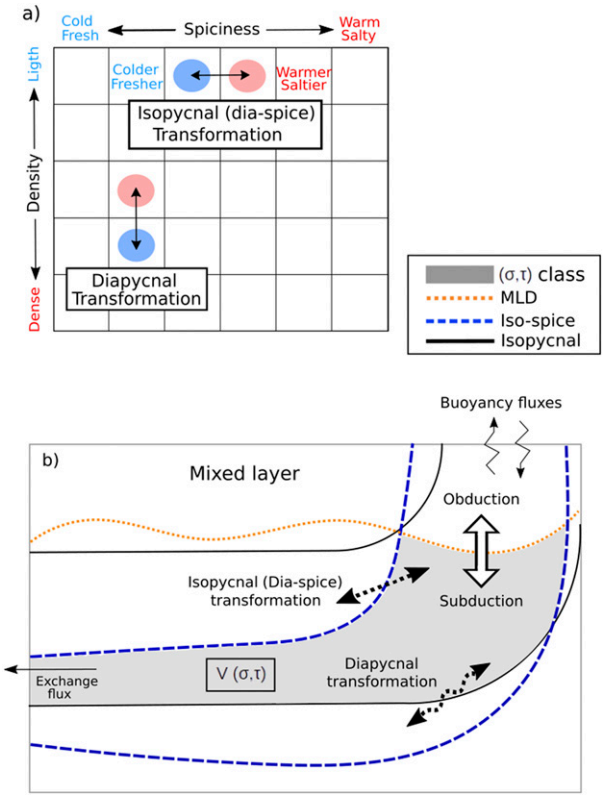

FIG. 1. (a) Diagram showing the effect of the transformation of a given water class in σ–τ space, and (b) processes involved in the volume change of a given σ–τ class in geographical coordinates.

the linear vorticity balance (Sverdrup balance) as follows:

$$w_H = w_{\mathrm{Ek}} + \frac{\beta}{f}\int_{-H}^{0} v\,dz, \tag{3}$$

where w_{Ek} is the Ekman pumping and β is the gradient of the planetary vorticity f.

The eddy-induced subduction is also a vertical term since it is defined as the horizontal divergence of the eddy bolus transport [last right-hand term of Eq. (2)]. However, in this study and following the procedure of Sallée et al. (2010), the eddy-induced subduction will be considered apart from the vertical velocity term. This differentiation allows a better understanding of the dynamics behind the different subduction terms. Following Sallée et al. (2010), $U_H^{\mathrm{ed}} = u_h^{\mathrm{ed}} H$ can be parameterized as

$$U_H^{\mathrm{ed}} = \frac{\partial}{\partial z}(k\mathrm{sl}), \tag{4}$$

where k is the eddy diffusion coefficient: $k(z) = k_{\mathrm{MLb}}[N^2(z)/N^2_{\mathrm{MLb}}]$ (with k_{MLb} being the diffusion coefficient at the base of the mixed layer and N^2 being the Brunt–Väisälää frequency), "sl" is the slope of the isopycnals ($=\nabla_h b/b_z$), b is buoyancy ($=g\sigma/\sigma_0$), g is the gravity acceleration, and σ and σ_0 are the density and reference density, respectively. A first attempt was made to compute observations-based eddy-induced subduction by obtaining U_H^* as in Eq. (4). However, as both the second horizontal and vertical derivative of density computed from our dataset result in a too-noisy field, it was impossible to obtain a reliable estimation of U_H^{ed}. In consequence the eddy-induced subduction was computed by using the bolus velocity obtained from ECCOv4, which is constructed by means of the parameterization proposed by (Danabasoglu et al. 1994). The computation of the lateral induction from both ECCOv4 and ISAS products gives consistent results (see Fig. S3 in the online supplemental material).

b. *Water-mass transformation*

The method used here to compute water-mass transformation in the σ–τ coordinates is based on the thermohaline derivation of Evans et al. (2014) from the equations of tracer conservation:

$$\partial C/\partial t = \underbrace{-\mathbf{u}\cdot\nabla C}_{\text{Advection}} + \underbrace{k\nabla^2 C}_{\text{Diffusion}} + f_C, \tag{5}$$

where k is the diffusion coefficient and $f_{\mathbf{C}}$ represents any source or sink of the given tracer C. Similar to their equations, the transformation across σ and τ surfaces is respectively expressed as

$$U_\sigma(\sigma,\tau) = \int_{\sigma'=\sigma} \Pi(\tau,\tau')u_\sigma\,dA \quad \text{and} \tag{6a}$$

$$U_\tau(\sigma,\tau) = \int_{\tau'=\tau} \Pi(\sigma,\sigma')u_\tau\,dA, \tag{6b}$$

where $\mathbf{\Pi} = 1$ if σ and τ are within the given σ–τ class [σ', τ', where $\sigma' = (\sigma \pm \Delta\sigma/2)$ and $\tau' = (\tau \pm \Delta\tau/2)$] and $\mathbf{\Pi} = 0$ otherwise. Here, u_σ and u_τ are respectively the diapycnal and diaspice velocity components and dA are the isopycnal [Eq. (6a)] and isospice [Eq. (6b)] areas covered by the given τ–σ class limits. The volume change within a given σ–τ class can then be expressed following Eqs. (1), (2), and (6) as

$$\left(\frac{dV}{dt}\right)_{(\sigma',\tau')} = S_{(\sigma',\tau')} + U_\sigma(\sigma',\tau) + U_\tau(\sigma,\tau') + \Psi_{(\sigma',\tau')}. \tag{7}$$

As expressed in Eq. (7), the method of Evans et al. (2014) was modified to include the previously computed subduction in the transformation equation. This modification was made to assign to the diasurface

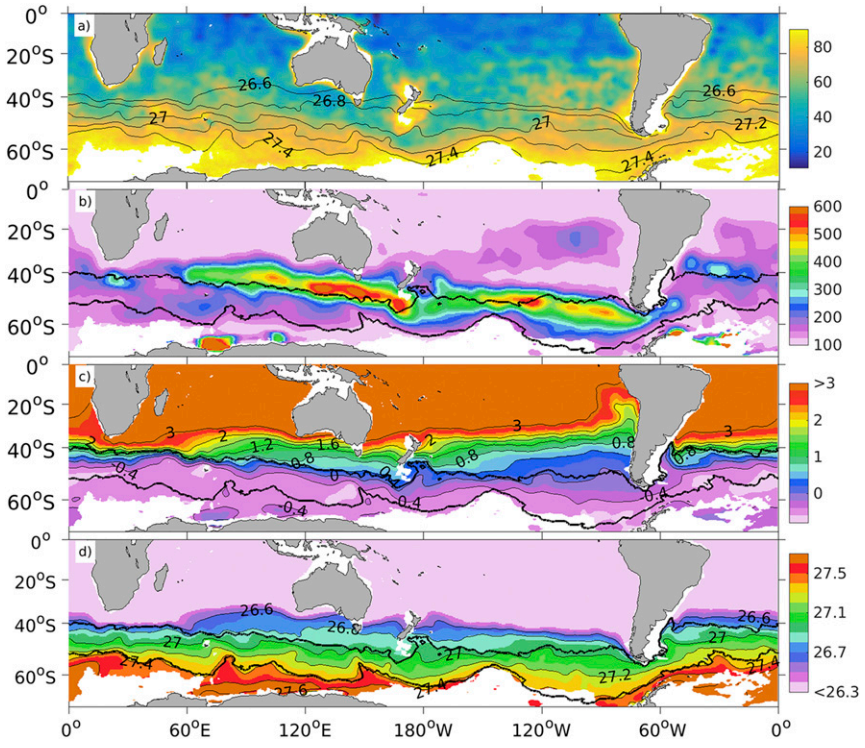

FIG. 2. (a) Percentage of variance averaged between 2006 and 2015 obtained from ISAS. (b) Depth of the deepest mixed layer over the 10-yr sampling period. (c) Spiciness and (d) potential density at the MLD. Colors are saturated in regions where $\tau \geq 3$ and $\sigma < 26.5\ \mathrm{kg\ m^{-3}}$, which are not the focus of this study. The thick lines in (b)–(d) represent the northern and southern boundaries of the ACC computed as the outermost closed contours of sea surface height (obtained from the Copernicus Marine environment monitoring service) through the Drake Passage.

transformations and exchange flow only the volume change that is not accounted for by subduction. To solve Eq. (7) for the unknown transformation and exchange flow terms, we constructed a set of linear equations that link the volume trend to the interior water-mass transformation in σ–τ coordinates:

$$\frac{dV}{dt} - S = \mathbf{A}\mathbf{x}, \tag{8}$$

where $\mathbf{A}$ is the matrix of coefficients of the linear equations and $\mathbf{x}$ is the vector of the resulting diasurface transformations and exchange flux: $\mathbf{x} = (U_\sigma + U_\tau + \Psi)$. This equations system is solved by means of a least squares regression. Because of its underdetermined nature, the equations system has multiple least squares solutions; therefore, we used the minimum norm solution to pick out the solution with the smallest $||x_2||$, which is unique by definition. The residuals or relative errors, computed as $|[(dV/dt) - S] - \mathbf{A}\mathbf{x}|/|[(dV/dt) - S]|$ were on average of order 10^{-11}, with a maximum at 10^{-5}.

The resulting $\mathbf{x}$ was then decomposed into the transformation across spiciness and density surfaces and the exchange flux across the geographical domain. The matrix dimensions as well as the very detailed procedure can be found in Evans et al. (2014).

4. Results

a. *Mean features of the Southern Hemisphere oceans*

The mean percentage of variance over the sampling period obtained from the ISAS optimal interpolation (Fig. 2a) is a proxy of the measurement network sampling in the SHOs. High or low values of the percentage of variance indicate that no new data or many new data, respectively, have been added to the background first guess, which in the case of ISAS is the climatology over the period 2005–12.

High percentage of variance, related with less sampled regions, can be observed within the southernmost latitudes. Values greater than 90% were blanked as an ad hoc limit to illustrate where the results would not be

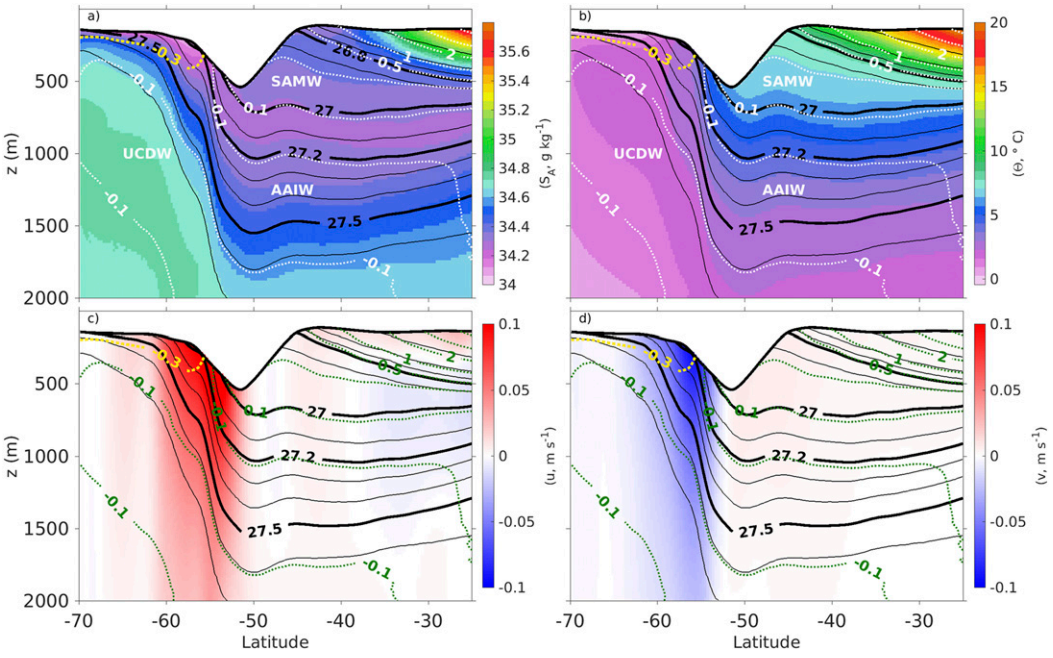

FIG. 3. Vertical section below the MLD of (a) S_A, (b) Θ, (c) zonal velocity, and (d) meridional velocity between 25° and 70°S at 130°W. White [green in (c) and (d)] dashed lines are the isospiciness contours, and black solid lines represent the isopycnals. The yellow isospiciness dashed line of −0.3 differentiates AAIW and AAWW. The thick black density contours represent the limits of the SAMW and AAIW.

reliable as computed from data only. Most of the blanked area corresponds to seasonally sea ice–covered regions with few available data (Pellichero et al. 2018). The deepest MLDs over the period 2006–15 (Fig. 2b) is associated with the northern boundary of the ACC, mainly in the southern Indian and Pacific basins with maxima (exceeding 600-m depth) south of Australia and in the central southern Pacific.

Note that in this study we will only focus on the waters ranging between $\sigma = 26.3$ and $27.5\,\mathrm{kg\,m^{-3}}$ and having $\tau = -0.6$–3, which meet the criteria of having a good sampling resolution, showing significant trends ($p < 0.05$), and being fully represented within the first 2000 m of the water column. It is noteworthy that some of the waters studied here extend further north in the ocean interior to, at least, the equator and that is the reason to refer to the SHOs instead of restricting to the Southern Ocean.

The strongest density and spiciness gradients on the MLD are found in the Atlantic and western Indian basins at the northern boundary of the ACC (Figs. 2c,d). While the meridional density gradient is relatively smooth from $\sigma = 26.8$ to $27.4\,\mathrm{kg\,m^{-3}}$ (Fig. 2c), there is a strong spiciness gradient between $\tau = -0.2$ and $\tau = 3$ (Fig. 2d).

The main water masses involved in this study and their characteristics are shown in a vertical section at 130°W (Figs. 3a,b), chosen as a key location that is representative of the SAMW and IW. In the southeastern Pacific (SEP), at $\sigma = 26.9$–$27\,\mathrm{kg\,m^{-3}}$, the SEPSAMW is well recognized by its relative low stratification and great volume in comparison with the surrounding waters (Naveira Garabato et al. 2009; Piola and Georgi 1982; Aoki et al. 2007; Hanawa and Talley 2001; Cerovečki et al. 2013). SEPSAMW is characterized in Figs. 3a and 3b between $\tau = 0.1$ and $\tau = 0.3$ (i.e., τ class of 0.2) with $\Theta = 6.3°$–7.4°C and $S_A \sim 34.4\,\mathrm{g\,kg^{-1}}$.

Because of the longitudinal variations of the salinity minimum characteristic of the AAIW, the definition of its upper density limit varies in the literature between $27.0\,\mathrm{kg\,m^{-3}}$ (Sallée et al. 2010; Abernathey et al. 2016) and $27.2\,\mathrm{kg\,m^{-3}}$ (Piola and Georgi 1982; Naveira Garabato et al. 2009; Badin et al. 2013). In this study, based on the coherent structure found in the σ–τ and geographical coordinates AAIW has been described by a density between 27.2 and $27.5\,\mathrm{kg\,m^{-3}}$ at the τ class of −0.2, which corresponds approximately to $\Theta \sim 2°$–4°C and $S_A \sim 34.3$–$34.5\,\mathrm{g\,kg^{-1}}$. The waters lying between the 27.0 and $27.2\,\mathrm{kg\,m^{-3}}$ isopycnals have characteristics typical of the SAMW (a low stratified thick core). They are mainly found in the southeastern Pacific where, at spiciness values between −0.2 and 0, they conform the densest variety of SEPSAMW. At the easternmost limit, near the Drake Passage, these dense

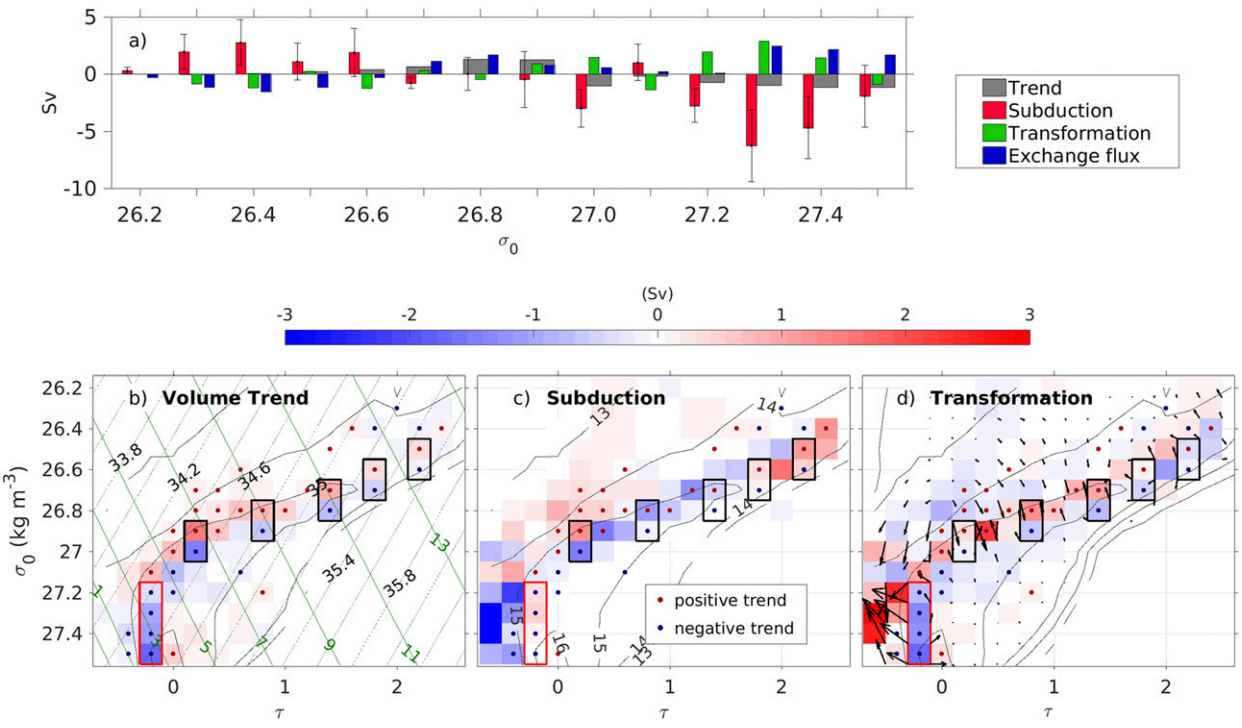

FIG. 4. (a) The τ integral of volume trends, subduction, transformation, and exchange flux rates over the period 2006–15 in density classes. Error bars associated with subduction are displayed. (b) Volume trends in σ–τ coordinates; only significant trends are marked with dots according to the legend. Green and dashed, black contour lines are the Conservative Temperature and Absolute Salinity, respectively. (c) Mean subduction in σ–τ coordinates, where red colors indicate subduction and blue colors indicate obduction. (d) Mean water formation (colors, where red is for formation and blue is for destruction) and transformation (arrows). Gray contour lines are the $\log_{10}$ of the total volume. For clarity, SAMW squares are outlined in black and AAIW in red.

SEPSAMW can be also considered as a transition layer between SAMW and AAIW.

AAIW is found poleward of 25°S, its structure changes considerably along the meridional section. It is linked to the strong meridional σ–τ (and Θ–S_A) front coincident with the deepest MLD and the eastward flux of the ACC between 50° and 60°S (Fig. 3c). North of this front the AAIW comprises a thick layer extending between 1000- and 1500-m depth while south of the front a squeezed and shallow AAIW is found as the isopycnals shoal and reach the MLD. At this location, the AAIW properties shift toward fresher ($S_A \sim 34.2$–$34.4\,g\,kg^{-1}$) and colder ($\Theta \sim 1.1$°–2.8°C) conditions. Those conditions are the signature of the AAWW evidenced by a decrease of the spiciness to $\tau < -0.3$ in the thin layer below the MLD. Under the AAWW, a strong density gradient gives way to the denser ($\sigma > 27.6\,kg\,m^{-3}$) UCDW characterized by a great volume of nearly constant properties ($\Theta \sim 1$°C; $S_A \sim 34.7\,g\,kg^{-1}$) centered at $\tau = -0.1$.

Figure 3d shows an important feature of the ACC: at this particular location, the mean meridional and zonal components of the velocity are of very similar magnitude, indicating the presence of a standing meander. Meanders, ubiquitous along the ACC are key for the occurrence of lateral induction, and, therefore, they play a key role in our study.

b. *Volume budget*

The τ integral (over the τ classes between -0.6 and 3) of the decadal volume trends, subduction, (trans) formation and exchange flux rates along every density class are shown in Fig. 4a. The most remarkable pattern is the subtle general lightening of the interior mode waters in the last decade evidenced by the increasing volume of the upper layers ($\sigma < 27\,kg\,m^{-3}$; $+4$ Sv) in detriment to the lower ones ($\sigma \geq 27\,kg\,m^{-3}$; -6.5 Sv).

While the net water-mass formation does not show a consistent pattern, net obduction occurs within the densest waters classes ($\sigma \geq 27.2\,kg\,m^{-3}$) and subduction occurs within the lightest ones ($\sigma \leq 26.6\,kg\,m^{-3}$). Subduction between the density classes of 26.7–27.1 $kg\,m^{-3}$ (SAMW range) shows a random behavior that cannot be unraveled by using density coordinates only. Volume trends, subduction, and interior formation rates are of the same order of magnitude. Obduction seems to

drive the negative IW volume trends at σ = 27.2–27.5 kg m^{-3}, whereas the relationship between SAMW and subduction is not clear from a τ-integrated point of view Fig. 4a.

The exchange flux is important in the lighter density classes where it balances the water formation by subduction with a flow out from the domain, presumably across the equator. Within the densest classes, a flow from the south seems to enter the domain and partly compensates the strong volume loss by means of obduction. The exchange flux also seems to play a role on the volume change between the density layers of 26.7 and 27 kg m^{-3}. However, this terms is important over the spicier waters near the equator, away from the SAMW core (not shown). A more detailed view of the isopycnal and diapycnal transformation as well as the exchange flux in σ–τ coordinates is shown in the online supplemental material (see Fig. S4).

To get more insight in the driving mechanism associated with specific water masses we show the σ–τ decomposition of the volume trends (Fig. 4b), subduction (Fig. 4c) and formation and transformation rates (colors and arrows respectively in Fig. 4d). From this decomposition two striking features arise. The first one is the existence of σ classes with the same spiciness (τ = 0.2, 0.8, 1.4, 1.8, and 2.2) and opposed volume trends of similar magnitude that will be referred to as two-layer density structures. All these structures lay on the SAMW density range along the SHOs, between σ = 26.8–27.0 kg m^{-3} and τ = 0–0.4 in the South Pacific and between σ = 26.5–26.8 kg m^{-3} and τ = 0.8–2.2 in the South Indian and South Atlantic basins (not shown).

The upper layers of the SAMW [from now on, (U)SAMW] show positive volume trends (Fig. 4b). From a σ–τ perspective, these trends are either correlated with subduction (Fig. 4c) or with diapycnal transformation (Fig. 4d, see also Fig. S4 in the online supplemental material). A good example is the case of the SEPSAMW, the mode water with the strongest trends. Within the lightest type of SEPSAMW (σ = 26.9 kg m^{-3} and τ = 0.2) subduction accounts for 1.2 Sv of the 1.5 Sv of volume gain over the last decade. On the contrary, and with the exception of the less dense SEPSAMW where obduction (−1.4 Sv) is the main responsible for the volume loss (−1.5 Sv), the negative volume trends of the lower layers of the SAMW [from now on, (L)SAMW] seem not to be well correlated with obduction. Instead, the (L)SAMW is subjected to a negative transformation (Fig. 4d) that accounts for most of the volume loss (Fig. 4b). Within the (U)SAMW, and despite the importance of subduction in the volume gain, transformation is also to be considered. In the case of the (U)SAMW at σ = 26.7 and 27.8 kg m^{-3} transformation accounts for approximately the same proportion of volume change as subduction, with the main contribution being from the isopycnal component (+0.9 and +0.7 Sv respectively). The most notorious case is that of the densest type of SEPSAMW (σ = 27 kg m^{-3} and τ = 0) where the volume gain (0.7 Sv) is almost fully driven by transformation (~0.9 Sv).

The second striking feature in Fig. 4b is a strong negative volume trend over the AAIW density range (σ = 27.2–27.5 kg m^{-3} at τ = −0.2). Surprisingly, this net volume loss (−4.1 Sv) coincides with a weak subduction rate (+1 Sv) across the whole AAIW τ class (Fig. 4c) and the volume loss is driven by strong negative isopycnal transformation (−10.3 Sv). This transformation crosses the τ = −0.3 and the τ = −0.5 surfaces toward the colder and fresher AAWW (Fig. 4d). The net interior formation of AAWW by transformation and positive exchange flow is then compensated by strong obduction (−16 Sv; Fig. 4c) back into the mixed layer, which results in a slight net volume loss (−0.6 Sv). Within the densest layers of the AAIW (27.4 and 27.5 kg m^{-3}) there is also some transformation toward warmer and saltier (spicier; τ = 0) IW. This formation of the spiciest IW (Fig. 4d) produces a significant volume gain of its 27.5 kg m^{-3} density class over the last decade.

To get more insight in the identification of the subduction hot spots in relation with the volume trends over the last decade, we show in Fig. 5 the spatial distribution of the mean subduction and its three components as detailed in Eq. (2). Subduction shows high spatial variability, the subduction/obduction hot spots reach rates of up to 1000 m yr^{-1} and they are widespread along the Southern Ocean, mainly within the ACC limits. The most obvious hot spots appear as dipolar or rather multipolar structures placed between the East of Australia and New Zealand, as well as in the central South Pacific. Those structures are evident in the lateral induction term (Fig. 4a) and they coincide with the narrowing of the ACC flow (blue lines). This suggests that they are topographically induced features (Langlais et al. 2017) where the role of the MLD horizontal gradient is minimized in comparison with the velocity field. Away from these hot spots, subduction magnitude decreases considerably to values lower than 500 m yr^{-1}.

Subduction is mainly shaped by the lateral induction south of 40°S (Fig. 5a) while north of 20°S the vertical term, dominated by the Ekman pumping (not shown), is the main contributor to the total subduction (Fig. 5c). The eddy-induced term is the dominant between these two regions (between 20° and 40°S),

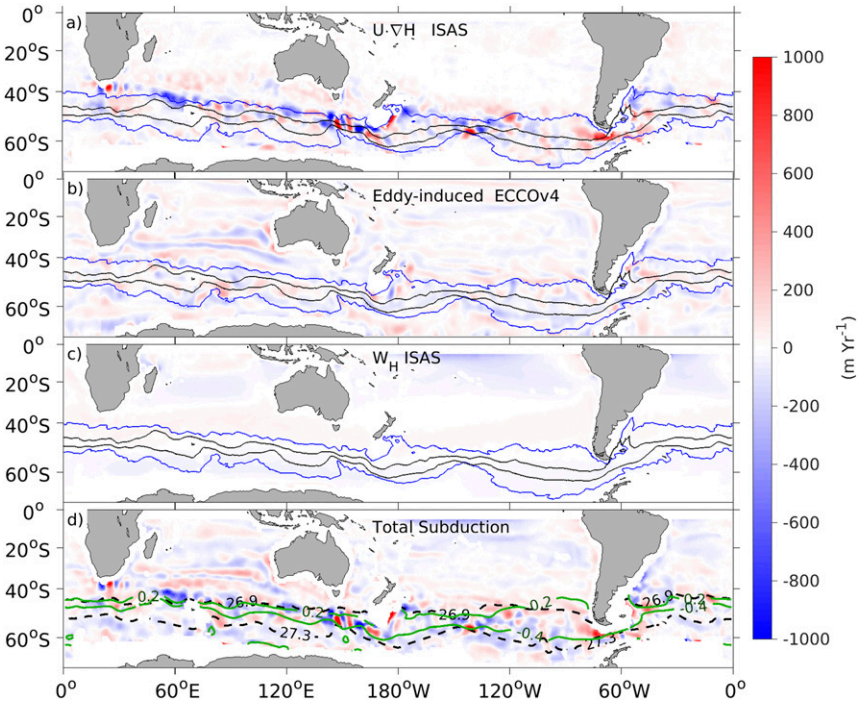

FIG. 5. Components of subduction as described in Eq. (2): (a) lateral induction, (b) eddy-induced subduction, (c) vertical velocity, and (d) total subduction as the sum of the three terms. Black contours in (d) are the 26.9 and 27.3 kg m^{-3} isopycnals, and green contours are the 0.2 and −0.4 isospice at the base of the deepest MLD. Blue contours in (a)–(c) represent the northern and southern boundaries of the ACC computed as the outermost closed contours of sea surface height through the Drake Passage. The black lines inside are the Subantarctic and Polar Fronts from north to south, respectively, as computed by Sallée et al. (2008).

however, its influence extends to the whole region as it is responsible for small-scale variability (Fig. 5b).

c. SAMW

The two-layer density structures in Fig. 4b are not continuous features along the spiciness dimension, rather they represent particular locations of high variability of the SAMW volume. Figure 6 shows the spatial distribution of thickness (colors) and minimum depth (contours) (Figs. 6a,b), subduction (Figs. 6c,d) and volume trend (Figs. 6e,f) of the two density layers with opposed trends of the lightest type of SEPSAMW (σ = 26.9–27.0 kg m^{-3} and τ = 0.2). The volume time series for each layer are shown in (Fig. 6g). The SEPSAMW comprises the densest and less spicy type of SAMW. The upper layer is found in the southeastern Pacific between 100- and 600-m depth, its core is 300 m thick and centered around 120°W (Fig. 6a). The thickness of the lower layer's core is around 200–250 m, located in the central South Pacific between ~20° and 45°S and between 100° and 170°W (Fig. 6b). Although both layers of the SEPSAMW are distributed all around the Southern Ocean, their cores and trends are well defined and restricted to a smaller region in the eastern and central South Pacific.

Subduction rates associated with the upper layer of the SEPSAMW (Fig. 6c) show high spatial variability, however, a subduction hot spot is evident at the core of thickness and trend location (Figs. 6a,e), centered at 120°W and 45°S. In contrast, and despite the apparent agreement between volume trend and obduction within this σ–τ class in Fig. 4, for the lower layer of the SEPSAMW the spatial distribution of obduction (Fig. 6d) has no evident correlation with the negative volume trend (Fig. 6f). The volume time series of both SEPSAMW layers (Fig. 6g) are strongly negatively correlated ($r \sim -0.9$, with $p \sim 0$), which suggests isopycnal heaving between the two layers.

d. Intermediate waters

The AAIW is ubiquitous in the SHOs between 30° and 60°S reaching 70°S in the South Pacific basin. Across its density range (27.2–27.5 kg m^{-3}) AAIW occupy a thick layer of the water column between 200 m depth in the southernmost location and ~1400 m north of the ACC. The maximum thickness of ~850 m is found in the

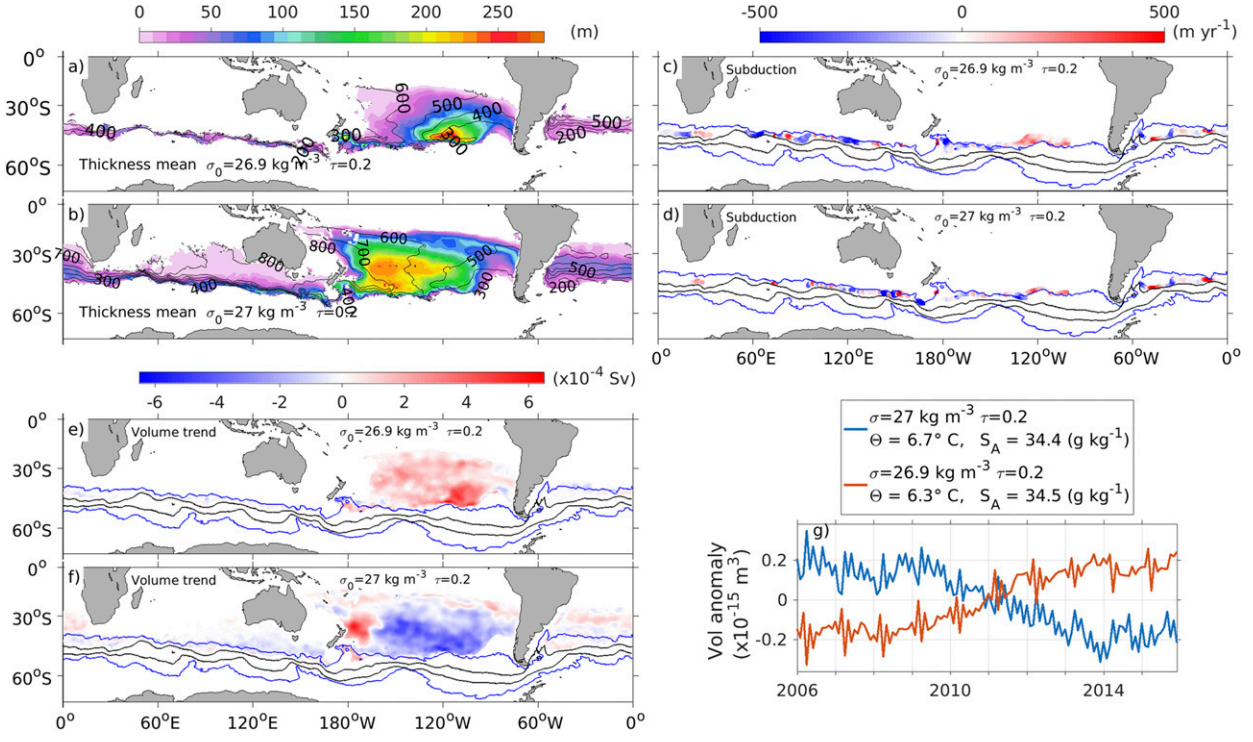

FIG. 6. Geographical location of the thickness (colors) and minimum depth (contours) for the (a) upper ($\sigma = 26.9\,\mathrm{kg\,m^{-3}}$) and (b) lower ($27.0\,\mathrm{kg\,m^{-3}}$) layer of the SEPSAMW at $\tau = 0.2$. (c),(d) Subduction rate for the two respective density layers. Red color indicates subduction into the thermocline. (e),(f) Geographical distribution of the volume trend for the respective density layers. (g) volume time series. Blue contours in (c)–(f) represent the northern and southern boundaries of the ACC computed as the outermost closed contours of sea surface height through the Drake Passage. The black lines inside are the Subantarctic and Polar Fronts from north to south, respectively, as computed by Sallée et al. (2008).

Southeastern Pacific and the South Atlantic basins (Fig. 7a). The spiciest AAWW class ($\tau = -0.4$, the one showed in Fig. 7) overlies the southernmost portion of the AAIW between ~40° and 70°S. It lays approximately between 100 and 600 m depth reaching 800 m in the Atlantic basin (Fig. 7b) where the slope of the isopycnals is the greatest (not shown). It is a relatively thin water mass, the thickest layer of which barely reaches 300 m.

AAIW shows a negative volume trend (Figs. 7b,e) with variable zonal and meridional distribution. North of the ACC the strongest volume loss occurs in the South Indian and South Atlantic basins, while in the South Pacific the volume trend is smaller and with an unclear spatial pattern. Southward, within the ACC, the previous pattern reverses: the main negative trends are located in the South Pacific basin and through the Drake Passage (Fig. 7e) while in the Atlantic and Indian basins the volume increases (Fig. 7e) mainly between the Subantarctic and Polar fronts with a complementary AAWW volume loss (Fig. 7f).

The subduction rate within the AAIW is slightly positive (Fig. 4c) and very localized (Fig. 7c) while, in contrast, the fresher and colder AAWW is subject to strong obduction (Fig. 4c). This obduction occurs mainly along the ACC in the South Pacific basin (Fig. 7d) and south of the ACC in the South Indian basin.

The temporal variability of the AAIW volume (Fig. 7g) shows similar behavior at all the density layers over the last decade; between 2006 and 2010 the trend is null, but from 2011 to 2016 there was a change toward strong negative trends that range between 1.5 and 3 Sv from the lightest to the densest layer (not shown). The causes of the interannual variability of the trend are not addressed in this study.

e. Overview

A more detailed insight into the relative contribution of each term driving the volume budget is shown in Fig. 8 for the SAMW (Fig. 8a), AAIW and the spiciest AAWW ($\tau = -0.4$) (Fig. 8b) as the integral of every term of the volume budget over their geographical location given by the σ–τ limits.

While the lateral induction term can be large in localized hot spots, spatial integration over a given σ–τ class results in a cancellation of the positive/negative lateral

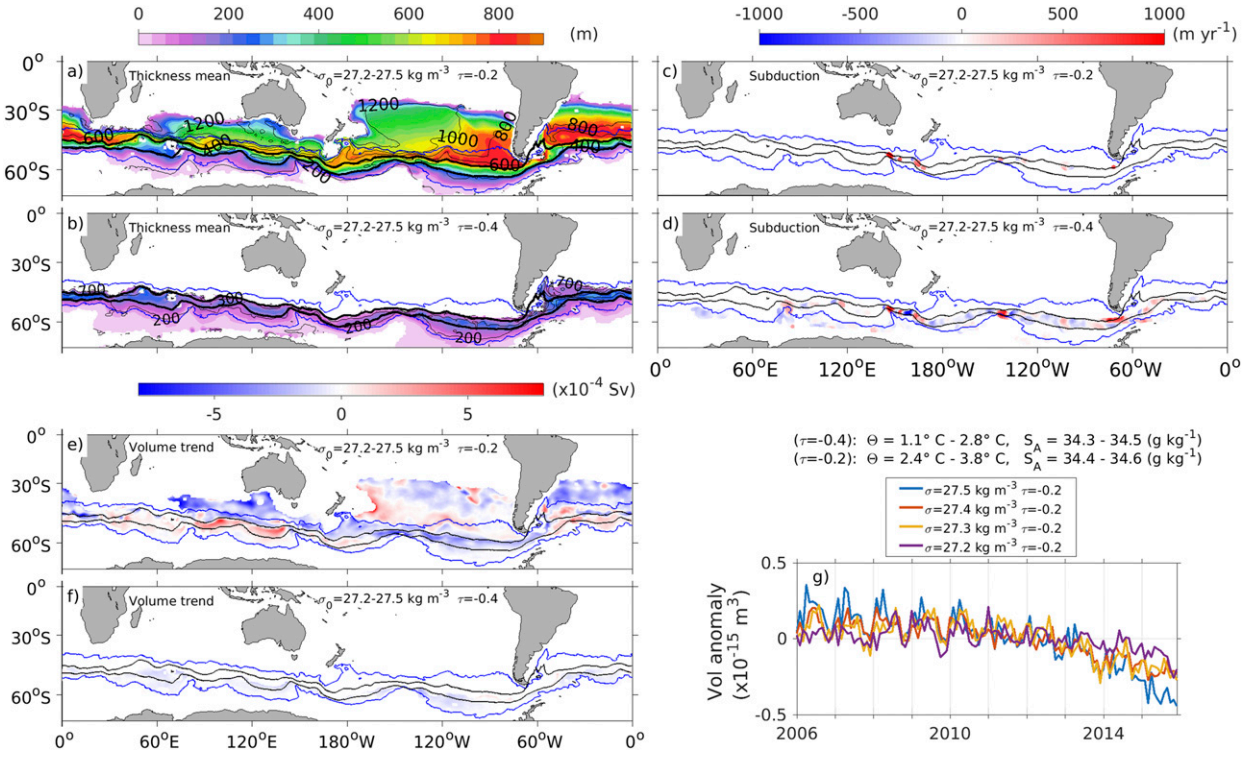

FIG. 7. As in Fig. 6, for $\sigma = 27.2$–$27.5\,\mathrm{kg\,m^{-3}}$ and (a),(c),(e) $\tau = -0.2$ (AAIW) and (b),(d),(f) $\tau = -0.4$ (AAWW). (g) Volume time series only for the AAIW classes, i.e., the ones with a significant volume trend.

induction patches. It is somehow striking how after this integration, the lateral induction opposes the volume gain within all the SAMW classes excluding the densest variety of SEPSAMW. As a result, the vertical velocity term is actually the largest subduction term in the spatial integral for most SAMW classes.

Diapycnal transformation from the lower to the upper layers of the SAMW is evident at the τ classes of 1.4, 0.8, and 0. Within those spiciness classes, a combination of diapycnal and isopycnal transformation drives the volume loss within the (L)SAMW (Fig. 8a) with contribution of lateral induction only at the SEPSAMW (Fig. 8a).

In the case of the IW, the driving mechanisms are very similar between the different density classes. As mentioned before, the destruction of AAIW is largely driven by isopycnal transformation ($-5\,\mathrm{Sv}$, Fig. 8b) that increases progressively with density. As result, a similar total amount of isopycnal transformation ($+4\,\mathrm{Sv}$) is driving the AAWW volume gain. Notably, the water destruction by negative transformation over the two densest AAIW layers (27.4 and $27.5\,\mathrm{kg\,m^{-3}}$) exceeds in $\sim$1.1 and $\sim$1 Sv respectively, the volume of AAWW formed by positive isopycnal transformation at the same density layers. The remainder, is attributed to 1) the transformation from the AAWW into less spicy AAWW (τ class $= -0.6$) at $\sigma = 27.4\,\mathrm{kg\,m^{-3}}$ (Fig. 4d) and 2) to the transformation of AAIW toward spicier IW ($\tau = 0$) at $\sigma = 27.5\,\mathrm{kg\,m^{-3}}$. This is also visible in Fig. 4d where the arrows indicate isopycnal transformation from the class of $\tau = -0.2$ in both senses toward spicier and less spicy waters.

Within the AAWW, the final volume change is slightly negative due to a combination of eddy and Ekman induced subduction that balances the positive transformation (Fig. 8b). Finally, the exchange flux is only significant for the densest AAWW where it brings water into the domain ($+0.5\,\mathrm{Sv}$) from the southern limit and for the Indian SAMW where the net volume increases by means of an inflow from the Northern Hemisphere. To ensure the validity of our method, the red diamonds show the computed trend for each class. The volume change estimated directly and that obtained as the sum of all the contributing terms are coincident in all the cases. This was the expected result since, by construction, the transformation was computed to adjust to the other components and the residuals of this computation were negligible.

All of the previously described mechanisms driving the volume change of SAMW and IW are represented in Fig. 9 from a σ–τ (Fig. 9a) and latitude–depth perspective (Fig. 9b). The gray-shaded layers represent the

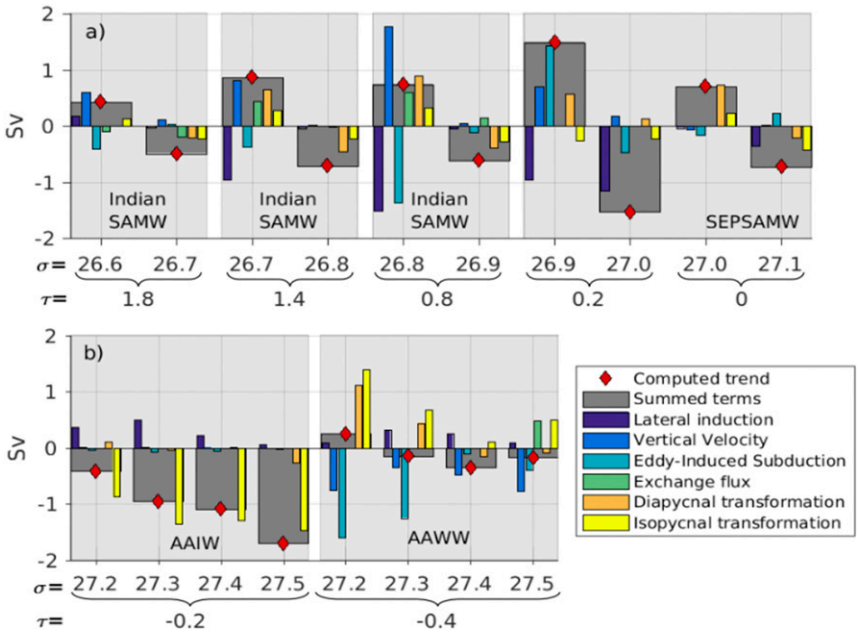

FIG. 8. Relative contribution of each subduction and transformation term to the total volume change for (a) the SAMW and (b) the AAIW and AAWW. Gray bars show the volume change as the sum of all terms, and the diamonds represent the computed volume trend.

waters out of the focus of this study, either for being partially unresolved within the first 2000 m of the water column or for the lack of significant trends. Waters colored in red gained volume while those in blue lost volume during the last decade. Figure 9b shows the schematic representation of the fluxes driving the water-mass volume changes in the real ocean, along a meridional section in the South Pacific basin. Note the existence of a strong spiciness gradient north of the ACC that is showed for the first time in this study. The transformation analysis in Fig. 4d showed the isopycnal flow from the AAIW across this spiciness surface into this spicier subtropical IW.

5. Discussion

Some studies on water-mass variability in the Southern Ocean are based in the identification of water-mass transformation in density coordinates only (Abernathey et al. 2016; Cerovečki et al. 2013; Katsumata et al. 2013; Marshall and Speer 2012; Pellichero et al. 2018; Tamsitt et al. 2018). Other studies on the same subject have been carried out in thermohaline coordinates (Evans et al. 2014, 2018; Hieronymus et al. 2014; Pemberton et al. 2015) and they identify more precisely the mechanisms driving the water-mass transformation in different regions and time scales. Here, we show that the averaging in density layers masks some of the variability among different water-mass types spreading along same isopycnal layer. These different types can only be distinguished by their T/S (or spiciness) change along isopycnals, as is notably the case of the IW. Our σ–τ approach analog to the thermohaline coordinates allows us to keep the more natural isopycnal framework for water-mass spreading as well as to readily identify the hot spots of volume change and their diabatic or adiabatic nature. Spiciness, the thermohaline variations along isopycnals, in addition to density, has shown to be an adequate variable to differentiate between different SAMW and IW types. This framework brings new insight on the distribution and variability of specific water masses.

Besides the differences associated to the coordinate system, the main novelty of this study resides in its method that is based on three stages. First, the hot spots of the volume change were identified and characterized. Second, the three main mechanisms driving the volume change in the interior ocean were diagnosed and estimated: subduction (or injection of volume to a certain water class), transformation (or change of the σ–τ class properties due to interior diasurface fluxes) and exchange flux across the domain's limits. Finally, we assessed the relative importance of the contributing terms of subduction and transformation to the total volume change in the water classes previously identified as the hot spots.

We are not addressing here the conditions under which the different water masses are formed at the

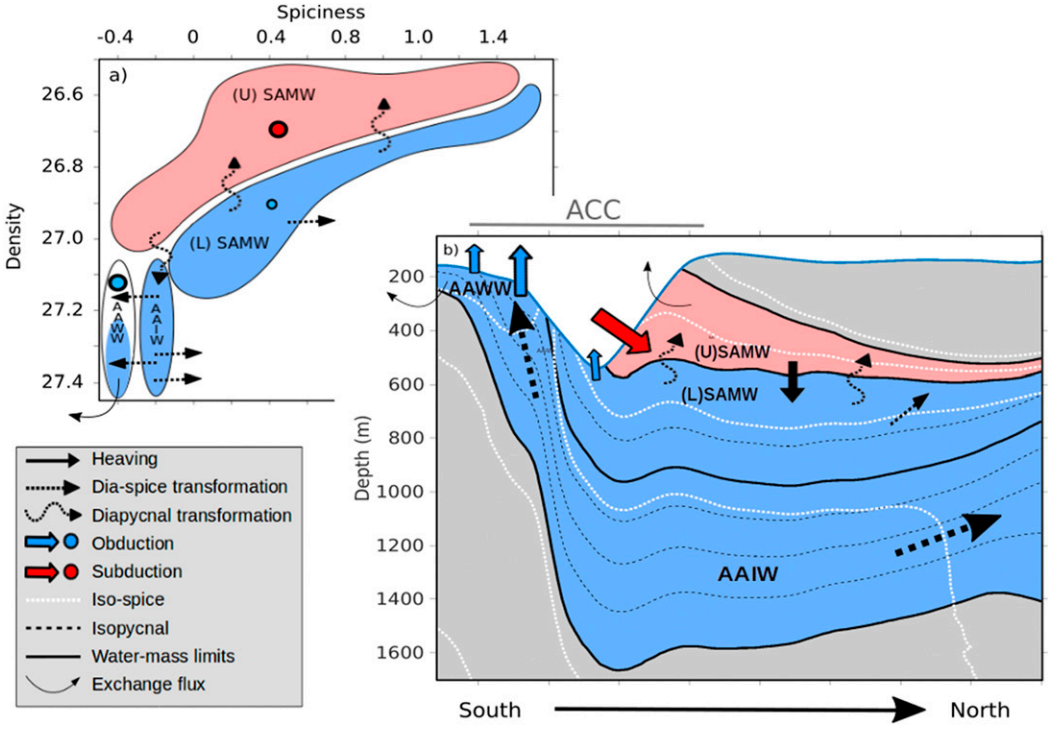

FIG. 9. Schematic of the fluxes driving the volume change in the SAMW and IW over the 2006–15 period in (a) σ–τ coordinates and (b) latitude–depth coordinates, showing a profile that is typical of the South Pacific.

surface. Instead, for the first time and using observations, we account for their evolution over the last decade (2006–15) once these water masses are retained in the interior oceans. In the following we provide a discussion on the dynamical and thermodynamical mechanisms driving the water-masses volume change and we hypothesize their relation with the changing atmospheric conditions in the SHOs.

a. SAMW

Mode waters in general, and the SAMW in particular are subjected to strong seasonal transformation in the mixed layer (Abernathey et al. 2016; Katsumata et al. 2013; Pellichero et al. 2018). We have documented here that while the interior SAMW is isolated from air–sea interactions it still exhibits important variability that has been retained at longer time scales and is driven by different mechanisms than its mixed-layer counterpart. The observed SAMW volume trends are characterized by two-layer density structures with the same spiciness and opposed trend sign; the upper layers gain volume while the lower layers loose it simultaneously and in a similar proportion. This feature together with the AAIW volume loss results in a lightening of the upper ocean layers that is in general agreement with the widely reported heaving-related warming in the Southern Ocean over the last decade (Gao et al. 2018; Häkkinen et al. 2016; Desbruyères et al. 2017; Kolodziejczyk et al. 2019).

The SAMW is known to be formed in the interior ocean by subduction (Hanawa and Talley 2001; Pellichero et al. 2018; Sallée et al. 2010). However, the correlation between an increasing volume and subduction rates of the (U)SAMW is not always evident in the σ–τ diagrams, which represent the integrated subduction over the whole distribution of the water classes. Although the large scale patterns of subduction agree with previous studies (Sallée et al. 2010; Tamsitt et al. 2018), our resulting subduction is characterized by complicated spatial structures at regional scale, where changes of sign occur within hundreds of kilometers. This spatial variability is especially evident in the lateral induction term where we observe noticeable multipolar subduction/obduction hot spots that are associated with the standing meanders of the ACC (Langlais et al. 2017). This patchy (positive/negative) spatial structure of subduction in geographical coordinates cancels when it is integrated in σ–τ classes. The result is an underestimation of the lateral induction mean magnitude for a particular σ–τ class. Therefore, the relative contribution of the lateral induction term (and this is extensive to the eddy-induced term), does not necessarily reflect the

local processes (Rintoul 2018) responsible for the volume change within the SAMW but a water-mass averaged variability. The opposite behavior is shown by the vertical velocity component of subduction, the relative importance of which is enhanced by the σ–τ integral because of the spatial continuity of its field. The geographical distribution of the properties and processes linked to the SEPSAMW and to the southeastern Indian SAMW (not shown) indicates that, indeed, subduction occurs at the water masses' core. This supports the general knowledge about the key role of subduction in SAMW formation (Hanawa and Talley 2001; Sallée et al. 2010). While the SAMW of a particular σ–τ class is extensively represented in geographical coordinates along the Southern Ocean (see, e.g., Fig. 6), its core and trend are confined to a particular region. Similar distribution patterns of the SAMW with very localized cores are reported by Kolodziejczyk et al. (2019). In their study, the core of the SEPSAMW is located slightly to the west from the one in this study, this is due to the shift of the density range considered in the plots [centered in 26.85 kg m^{-3} in Kolodziejczyk et al. (2019) and in 26.9 kg m^{-3} in the present study] and to the fact that we have selected only one spiciness class. Because mode waters involve low stratified water composing a considerable thickness of the water column, a small variation in the density layer implies a noticeable change in their distribution. This can be considered as a limitation of any discretization in density coordinates when addressing mode waters.

Related work on subduction in the Southern Ocean (Sallée et al. 2010) also shows subduction occurring at highly localized regions within the SAMW distribution, although their fields are smoother and therefore of lower magnitude. Despite the strong variability implied in the subduction computation and saving the differences in magnitude on their geographical distribution, our findings about the relative contribution of the subduction terms are largely in agreement with the results reported by Sallée et al. (2010). Similar magnitudes and small spatial-scale subduction features as those presented here, are reported in related studies carried out with models (Langlais et al. 2017; Downes et al. 2017)

While the implication of subduction in the SAMW formation is well known in literature, the σ–τ decomposition has provided new insight about the processes leading its variability. The net volume gained by the (U)SAMW produces by mass conservation a heaving of the underlying isopycnal, inferred by the strong negative correlation between the volume time series of the two density layers of the different SAMW. The volume loss within the (L)SAMW is driven by a combination of isopycnal and diapycnal water-mass transformation where the latter is directed from the lower to the upper density layer. Although obduction seemed important for the SEPSAMW in the σ–τ integral, the more detailed map of subduction shown in Fig. 6 does not show any evidence of correlation between the spatial distribution of obduction and the core of the maximum SEPSAMW volume trend.

Cerovečki et al. (2013) found, using an ocean state estimate, that an important amount of SAMW was destroyed by diapycnal mixing, although their study does not differentiate between mixed layer and interior waters. The importance of the diapycnal mixing is well known near the surface and near the bottom (Cerovečki et al. 2013; Rintoul 2018; Rintoul and Naveira Garabato 2013; Abernathey et al. 2016). In certain conditions, however, diapycnal mixing has been reported also at intermediate depths, between 500 and 1000 m (Naveira Garabato et al. 2004). Our results show important diapycnal fluxes between the two density layers of the different SAMW types that roughly corresponds with 400–600 m depth, meaning that the bottom influence is possible but not likely. The processes driving this transformation within the SAMW, far from the bottom and below the MLD, cannot be determined from the analyses performed here, however some hypothesis can be made to explain our results. The first one is based on the proximity of these water masses with the MLD. Rintoul (2018) stated that near the surface, the wind-generated, downward-propagating, inertial waves break, enhancing diapycnal mixing. This author does not limit this effect to the mixed layer, rather he suggests its presence in the upper SAMW (see his Fig. 3). A similar schematic representation places diapycnal mixing at intermediate depths in the study of Badin et al. (2013). Sloyan et al. (2010) found enhanced diapycnal diffusivity north of the Subantarctic Front below the mixed layer and these authors suggest that the energy required to maintain this diffusivity was supplied by a number of sources including wind forcing, mesoscale eddies and internal waves propagation. The second explanation relies in the dependence of the transformation computation on subduction. With the method used here to estimate transformation, an underestimation of subduction in a volume gain σ–τ class could result in an overestimation of transformation rates, including diapycnal mixing, this issue will be discussed further in section 5c. However, there is no known reason to suppose that diapycnal mixing could be preferentially overestimated over the isopycnal component.

A subduction–heaving–transformation sequence is proposed as the main mechanism driving the volume variability of the SAMW. Some studies on OHC (Häkkinen et al. 2015; Desbruyères et al. 2017; Kolodziejczyk et al. 2019)

have suggested this heaving as the dominant mechanism for the SAMW warming and as a proxy of subduction of warmed mixed-layer waters (Häkkinen et al. 2015). Wind forcing, through the increase in the wind stress curl has been found to be the main driver of the SAMW thickening (Gao et al. 2018). This is in agreement with our results in σ–τ coordinates, where the vertical subduction term was the main driver of the volume gain within all the (U)SAMW. However, the spatial distribution of the subduction terms as shown in Fig. 5 confirms that the lateral induction is locally important and is the main contributor to the subduction hot spots observed at the core of the SEPSAMW. Preliminary results showed that this is also the case of the South Eastern Indian SAMW (not shown). The eastward flow associated with the northern limit of the ACC together with strong zonal and meridional MLD gradients (Fig. 2b) are suggested to be responsible for the existence of the lateral induction hot spots and subsequent interior SAMW formation. Within the lateral induction term, and for all the density classes within the SEPSAMW (σ = 26.9–27 at τ = 0.2–0) the relative importance of the velocity field and the MLD gradient varies regionally. East and south of Drake Passage, where the densest type of SEPSAMW is formed, subduction seems to be dominated by the meridional excursions of the ACC due to the standing meanders (Langlais et al. 2017). In contrast, where the lightest SEPSAMW type is, the ACC keeps its zonal direction but crosses a pronounced MLD gradient (Fig. 2b). The locations where the ACC meanders play a key role on lateral induction are nicely showed by Langlais et al. (2017) (see their supplementary material).

Our results show that subduction and interior mixing are of the same order of magnitude and, in general both terms are important to explain the volume trends within the SAMW while the IW variability is driven by different processes that are discussed below.

b. *Intermediate waters*

The σ–τ decomposition provided a clear distinction between two types of IW at density between 27.2 and 27.5 kg m^{-3}: the AAIW ($\tau = -0.2$) and the fresher and colder AAWW ($\tau \leq -0.4$). Despite sharing density ranges, these two water masses show very distinctive features: they have opposed trends and different thermohaline characteristics but are connected by related dynamics. A third type of subtropical IW ($\tau = 0$) is also identified in this study, it limits with the AAIW in the North where both types of IW are connected by transformation fluxes at their densest layer.

Over the last decade, the main process involved in the strong AAIW volume loss has largely been the isopycnal transformation into the AAWW, placed on top and south of the AAIW. The isopycnal flux necessary to perform this transformation is thought to be accounted for by the eddy field associated to the ACC. As showed in the vertical section over the 130°W our results are consistent with the so-called eddy compensation (Marshall and Radko 2003; Marshall and Speer 2012); the eddy flux would be directed southward and upward along the sloping isopycnals crossing the $-0.3\,\tau$ surface that separates the AAWW from the AAIW. The main effect of this transport is a flattening of the sloping isopycnals. Considering the geographical distribution of the AAIW and AAWW volume trends and that isopycnal transformation is their main driving mechanism, we can infer that this isopycnal transformation from AAIW into AAWW is not a longitudinally homogeneous process. It occurs mainly in the South Pacific basin, around the Drake Passage and at some spots in the South Atlantic Ocean as those are the regions where the negative AAIW volume trends are found in an adjacent location to that of the AAWW. Moreover, the transformation of AAIW into spicier IW appears to have place all along the Southern Ocean, mainly in the South Atlantic and South eastern Indian basins and at the densest IW levels (σ = 27.4–27.5 kg m^{-3}) as showed by Fig. 4d. So far, we have not found a reason to explain this difference between the basins since eddy stirring takes place along the whole Southern Ocean (Naveira Garabato et al. 2011).

Numerical models and observations have revealed the dominant role that the mesoscale eddy field plays in controlling the response of the ACC transport to changes in wind stress (Meredith and Hogg 2006; Morrison and Hogg 2013). With the data that we have available it is not possible to make conclusions on the ultimate forcing responsible for the observed mechanisms driving the volume changes. The relatively short record used in this study has some important caveats affecting the consideration of the trends that need to be taken into account. For example, the sense and magnitude of the volume trends over the period 2006–15 can be very sensitive to the interannual and decadal variability. That said, we can hypothesize that the wind variability likely has a key role on the observed features. Stronger winds would produce, rather than an increase in the ACC mean transport, a higher EKE (Morrison and Hogg 2013; Gao et al. 2018; Marshall and Speer 2012). An increase in the EKE would increase the southward isopycnal transformation that would be consistent with the observed negative volume trend within the AAIW over the last decade. Besides the presence of important interannual variability, the progressive strengthen and variable shift of the wind field

have been largely documented in literature (Hogg et al. 2015; Langlais et al. 2017, among others). In particular, Hogg et al. (2015) reported an increase of the EKE in the South Pacific and South Indian basins since 1992, and a good correlation between the EKE and the wind stress.

Stronger winds would also cause an increase of the related northward Ekman transport. This is consistent with the observed subduction north of the ACC, which would partly explain the positive volume trend in the (U)SAMW over the last decade. However, subduction tends are not easy to identify, because the subduction hot spots can show important geographical variability as a result of the wind shift and concern different density layers over the time (Langlais et al. 2017).

Despite the strong positive transformation toward the AAWW, this water mass shows slight volume loss. A thin AAWW layer seats on top of the AAIW south of the subtropical density front in the ACC. Consequently, the outcropping of the IW isopycnals into the MLD mainly occurs within the AAWW range ($\tau < -0.4$) that is characterized by strong obduction. Zonal wind stress is known to induce upwelling poleward of the strongest wind zone (i.e., approximately between 45°S and the Subantarctic Front (Marshall and Speer 2012, see their Fig. 4a), which coincides with the region of AAWW outcropping. An increase of the average wind strength during the last decade would be in agreement with the average AAWW obduction. This is also consistent with the important contribution of the eddy field and the Ekman pumping to the total AAWW obduction as observed in this study and also reported Sallée et al. (2010). Ultimately, most of the trends and driving mechanisms observed in this study are in agreement with the reported increase in the wind strength over the last few decades (Meredith and Hogg 2006). However, the hypothesis about the wind stress as the ulterior driving forcing cannot be proved here and it needs further research for confirmation.

At seasonal scale, the AAWW is formed by winter mixing driven by excess of freshwater exported via the sea ice (Saenko et al. 2002; Abernathey et al. 2016) and destroyed in summer by transformation due to heat fluxes (Evans et al. 2018). Our results show that AAWW has an interior signature that remains beyond the mixed-layer seasonal transformations at interannual to decadal time scales. Even if it is in majority a thin layer, AAWW reaches up to 300 m of maximum thickness in the South Atlantic Ocean and it plays a key role in the understanding of the transformation/subduction processes driving the AAIW volume loss over the last decade.

As in the case of the SAMW, the processes leading the IW variability are not well represented by a zonal average as they are mostly local features (Sallée et al. 2010; Rintoul 2018). Strong subduction is found at very localized hot spots within the IW domain—for example, around the Drake Passage, which would agree with a local AAIW formation suggested by Talley (1996); however, the water-mass average indicates that a net AAIW volume loss is due to two different processes: 1) in the South Pacific and across all of the density layers there is an isopycnal transformation into AAWW, to be finally obducted back into the mixed layer, and 2) in the Atlantic and Indian basins, it is a northward isopycnal flux from the densest AAIW layers toward spicier subtropical/tropical IW. The dynamical explanation for this middepth flux remains to be addressed in future research.

c. *Considerations and limitations*

Despite the great improvement of the knowledge of the Southern Ocean since the Argo array implementation the amount of data available there remains still low in comparison with the northern regions. In addition, the Argo sampling rate is not high enough to resolve the eddy field associated with the ACC, which is known to be of key importance for the transport of tracers and properties distribution (Marshall and Speer 2012).

As computed from existing data, and due to the great amount of derivatives implied in the calculations, subduction has been subject to significant signal processing. In this sense, important MLD smoothing has been made to reduce the signal-to-noise ratio. The aim was to find a trade-off between obtaining interpretable results to explain the physics driving the water-mass formation, and keeping their reliability. In our approach the subduction is accounted for as the σ–τ integral over the geographical distribution of each class. While a particular water class can be widely distributed, the localized subduction spots at the SAMW cores are importantly contributing to their volume gain.

The water-mass transformation is an indirect estimation, it is constrained by, and depends on the volume trend and subduction. The resulting transformation is therefore also affected by uncertainty associated to σ–τ integrated subduction.

The time series, mainly of the upper SEPSAMW layer, shows an evident seasonal signal that is striking in the context of the interior waters. The MLD is a reference level, computed under variable criteria and in this case, subjected to smoothing that shoals the sharpest MLD features. As a consequence, it is likely that we are partly computing mixed-layer waters as interior waters with the subsequent assimilation of the seasonality contained in the mixed layer. After performing several tests, we decided to assume this limitation as it does not change the results significantly and the trade-off

between the benefits of smoothing and the presence of a remaining seasonal signal was largely positive.

In this study we have used potential density as the vertical coordinate due to the impossibility to obtain the spiciness from the more adequate neutral density. The latter is more accurate mainly to determine adiabatic mixing of properties in the ocean (McDougall 1987a). Although the difference between both variables can be significant in some locations, in upper waters (the first 2000 m at least) the isopycnals approximate the isoneutral surfaces very well (Sallée et al. 2008) and consequently we assume that the difference between them do no change our results and conclusions. In addition, we do not account either for cabbeling or thermobaricity (Groeskamp et al. 2016). These processes would produce a vertical advection as result of isopycnal mixing, however their vertical velocity is of the order $10^{-7}\,\mathrm{m\,s^{-1}}$ and the water-mass conversion they cause is comparable to that of the vertical diffusivity (McDougall 1987b). The σ–τ framework used in this study does not allow to account for these processes but rather, at large spatial scales we can consider them negligible in comparison with the other terms driving water-mass transformation.

Another important issue to consider is the spatio-temporal resolution of the dataset used in this study. The lateral induction term depends on the relative alignment of the horizontal flow and the lateral gradient in mixed layer depth and this relative alignment could depend on time scale. In Fig. S3 of the online supplemental material, we show that there are not important differences between the lateral induction term computed from monthly and climatological fields. We have also tested this computations with 3-day and monthly mean fields obtained from the NASA Jet Propulsion Laboratory ECCO2 Cube92 model output. The resulting lateral induction fields are comparable, with only minor difference (not shown). This suggests that, at least, at time resolution from 3-day average to climatological, the time scale has not a significant effect on the resulting subduction, however, we cannot test this hypothesis at finer time scales due to the lack of available model outputs. On the other hand, we have seen in this computation at higher spatial (0.25°) and temporal resolution that fine spatial-scale structures show up even after some degree of smoothing. Further sensitivity studies to fine space and time resolution on subduction computation should be carried out to assess the contribution of unresolved scale to subduction using in situ data products.

6. Summary and conclusions

For the first time, using mainly in situ observations, we addressed the variability of the SAMW and IW in the SHOs in the context of a changing ocean by accounting for the volume trend over the last decade. We were able to close the volume budget for the interior waters and to assess the relative contribution of the different mechanisms driving the volume change.

SAMW exhibits a two-layer density structure with the same spiciness but opposed volume trends over the last decade. Local subduction occurring at the SAMW cores, and diapycnal mixing from the lower layers mainly account for the volume gain of the (U)SAMW, while the lower layers lost a similar amount of volume by means of diapycnal and isopycnal transformation with only particular contribution of obduction.

The IW are driven by different dynamics than the SAMW. The AAIW, mainly in the South Pacific Ocean, lost volume during the last decade by means of strong isopycnal transformation into the colder and fresher AAWW that is finally obducted back into the mixed layer. The eddy field associated to the ACC is thought to be responsible for this transformation by transporting water upward and southward along the sloping isopycnals. In the Atlantic and Indian basins an isopycnal flux toward spicier (warmer and saltier) tropical IW from the densest AAIW layers also accounts for some of the volume loss during the last decade.

The addition of spiciness to the density coordinates allowed an accurate characterization of water masses spreading along isopycnals. Spiciness was a key variable to locate the SAMW in longitude along the South Pacific and Indian Oceans. Similarly, spiciness defines the latitudinal variations of the IW as it become fresher and cooler poleward. Finally, the σ–τ decomposition improved the understanding of the interior dynamics that govern the interior water-mass formation and transformation over the last decade.

Acknowledgments. Esther Portela was supported by CNES/INSU/Ifremer postdoctoral funding. This study was supported by the CNRS/INSU LEFE AcCOLADE project and CNES TOSCA SMOS OCEAN project in the framework of the ISAS project at LOPS SNO Argo-France. We thank Trevor McDougall for constructive discussions and the help provided with the MATLAB function to convert from density and spiciness to Conservative Temperature and Absolute Salinity. We also thank the two anonymous reviewers for their valuable comments that helped to improve this paper. ISAS15 is produced at LOPS as part of the Service National d'Observation Argo-France and is freely available (http://doi.org/10.17882/52367). This work is mainly based on the Argo dataset and thus benefited from the in-depth involvement of scientists and data managers with regard to

float deployment and data validation and distribution (http://www.argo.ucsd.edu/).

REFERENCES

Abernathey, R. P., I. Cerovecki, P. R. Holland, E. Newsom, M. Mazloff, and L. D. Talley, 2016: Water-mass transformation by sea ice in the upper branch of the Southern Ocean overturning. *Nat. Geosci.*, **9**, 596–601, https://doi.org/10.1038/ngeo2749.

Aoki, S., M. Hariyama, H. Mitsudera, H. Sasaki, and Y. Sasai, 2007: Formation regions of Subantarctic Mode Water detected by OFES and Argo profiling floats. *Geophys. Res. Lett.*, **34**, L10606, https://doi.org/10.1029/2007GL029828.

Badin, G., R. G. Williams, Z. Jing, and L. Wu, 2013: Water mass transformations in the Southern Ocean diagnosed from observations: Contrasting effects of air–sea fluxes and diapycnal mixing. *J. Phys. Oceanogr.*, **43**, 1472–1484, https://doi.org/10.1175/JPO-D-12-0216.1.

Böning, C. W., A. Dispert, M. Visbeck, S. R. Rintoul, and F. U. Schwarzkopf, 2008: The response of the Antarctic Circumpolar Current to recent climate change. *Nat. Geosci.*, **1**, 864–869, https://doi.org/10.1038/ngeo362.

Cerovečki, I., L. D. Talley, M. R. Mazloff, and G. Maze, 2013: Subantarctic Mode Water formation, destruction, and export in the eddy-permitting Southern Ocean state estimate. *J. Phys. Oceanogr.*, **43**, 1485–1511, https://doi.org/10.1175/JPO-D-12-0121.1.

Danabasoglu, G., J. C. McWilliams, and P. Gent, 1994: The role of mesoscale tracer transports in the global ocean circulation. *Science*, **264**, 1123–1126, https://doi.org/10.1126/science.264.5162.1123.

de Boyer Montégut, C., G. Madec, A. S. Fischer, A. Lazar, and D. Iudicone, 2004: Mixed layer depth over the global ocean: An examination of profile data and a profile-based climatology. *J. Geophys. Res.*, **109**, C12003, https://doi.org/10.1029/2004JC002378.

Desbruyères, D., L. McDonagh, and A. Elaine, 2017: Global and full-depth ocean temperature trends during the early twenty-first century from Argo and repeat hydrography. *J. Climate*, **30**, 1985–1997, https://doi.org/10.1175/JCLI-D-16-0396.1.

Dong, S., J. Sprintall, S. T. Gille, and L. Talley, 2008: Southern ocean mixed-layer depth from Argo float profiles. *J. Geophys. Res.*, **113**, C06013, https://doi.org/10.1029/2006JC004051.

Donners, J., S. S. Drijfhout, and W. Hazeleger, 2005: Water mass transformation and subduction in the South Atlantic. *J. Phys. Oceanogr.*, **35**, 1841–1860, https://doi.org/10.1175/JPO2782.1.

Donohue, K. A., K. L. Tracey, D. R. Watts, M. P. Chidichimo, and T. K. Chereskin, 2016: Mean Antarctic Circumpolar Current transport measured in Drake Passage. *Geophys. Res. Lett.*, **43**, 11 760–11 767, https://doi.org/10.1002/2016GL070319.

Downes, S. M., A. Gnanadesikan, S. M. Griffies, and J. L. Sarmiento, 2011: Water mass exchange in the Southern Ocean in coupled climate models. *J. Phys. Oceanogr.*, **41**, 1756–1771, https://doi.org/10.1175/2011JPO4586.1.

——, C. Langlais, J. P. Brook, and P. Spence, 2017: Regional impacts of the westerly winds on Southern Ocean mode and intermediate water subduction. *J. Phys. Oceanogr.*, **47**, 2521–2530, https://doi.org/10.1175/JPO-D-17-0106.1.

Evans, D. G., J. D. Zika, A. C. Naveira Garabato, and A. J. G. Nurser, 2014: The imprint of Southern Ocean overturning on seasonal water mass variability in Drake Passage. *J. Geophys. Res. Oceans*, **119**, 7987–8010, https://doi.org/10.1002/2014JC010097.

——, ——, ——, and ——, 2018: The cold transit of Southern Ocean upwelling. *Geophys. Res. Lett.*, **45**, 13 386–13 395, https://doi.org/10.1029/2018GL079986.

Flament, P., 2002: A state variable for characterizing water masses and their diffusive stability: Spiciness. *Prog. Oceanogr.*, **54**, 493–501, https://doi.org/10.1016/S0079-6611(02)00065-4.

Forget, G., J. M. Campin, P. Heimbach, C. N. Hill, R. M. Ponte, and C. Wunsch, 2015: ECCO version 4: An integrated framework for non-linear inverse modeling and global ocean state estimation. *Geosci. Model Dev.*, **8**, 3071–3104, https://doi.org/10.5194/gmd-8-3071-2015.

Gaillard, F., T. Reynaud, V. Thierry, N. Kolodziejczyk, and K. Von Schuckmann, 2016: In situ-based reanalysis of the global ocean temperature and salinity with ISAS: Variability of the heat content and steric height. *J. Climate*, **29**, 1305–1323, https://doi.org/10.1175/JCLI-D-15-0028.1.

Gao, L., S. R. Rintoul, and W. Yu, 2018: Recent wind-driven change in Subantarctic Mode Water and its impact on ocean heat storage. *Nat. Climate Change*, **8**, 58–63, https://doi.org/10.1038/s41558-017-0022-8.

Groeskamp, S., R. P. Abernathey, and A. Klocker, 2016: Water mass transformation by cabbeling and thermobaricity. *Geophys. Res. Lett.*, **43**, 10 835–10 845, https://doi.org/10.1002/2016GL070860.

Häkkinen, S., P. B. Rhines, and D. L. Worthen, 2015: Heat content variability in the North Atlantic Ocean in ocean reanalyses. *Geophys. Res. Lett.*, **42**, 2901–2909, https://doi.org/10.1002/2015GL063299.

——, ——, and ——, 2016: Warming of the global ocean: Spatial structure and water-mass trends. *J. Climate*, **29**, 4949–4963, https://doi.org/10.1175/JCLI-D-15-0607.1.

Hanawa, K., and L. D. Talley, 2001: Mode waters. *Ocean Circulation and Climate: A 21st Century Perspective*, G. Siedler et al., Eds., International Geophysics Series, Vol. 103, Academic Press, 373–386.

Hieronymus, M., J. Nilsson, and J. Nycander, 2014: Water mass transformation in salinity–temperature space. *J. Phys. Oceanogr.*, **44**, 2547–2568, https://doi.org/10.1175/JPO-D-13-0257.1.

Hogg, A. M. C., M. P. Meredith, D. P. Chambers, E. P. Abrahamsen, C. W. Hughes, and A. K. Morrison, 2015: Recent trends in the Southern Ocean eddy field. *J. Geophys. Res. Oceans*, **120**, 257–267, https://doi.org/10.1002/2014JC010470.

Huang, R., 2011: Defining the spicity. *J. Mar. Res.*, **69**, 545–559, https://doi.org/10.1357/002224011799849390.

Jackett, D. R., and T. J. McDougall, 1985: An oceanographic variable for the characterization of intrusions and water masses. *Deep-Sea Res.*, **32**, 1195–1207, https://doi.org/10.1016/0198-0149(85)90003-2.

Katsumata, K., B. M. Sloyan, and S. Masuda, 2013: Diapycnal and isopycnal transports in the Southern Ocean estimated by a box inverse model. *J. Phys. Oceanogr.*, **43**, 2270–2287, https://doi.org/10.1175/JPO-D-12-0210.1.

Kolodziejczyk, N., W. Llovel, and E. Portela, 2019: Interannual variability of upper ocean water masses as inferred from Argo Array. *J. Geophys. Res. Oceans*, **124**, 6067–6085, https://doi.org/10.1029/2018JC014866.

Langlais, C. E., A. Lenton, R. Matear, D. Monselesan, B. Legresy, E. Cougnon, and S. Rintoul, 2017: Stationary Rossby waves dominate subduction of anthropogenic carbon in the Southern

Ocean. *Sci. Rep.*, **7**, 17076, https://doi.org/10.1038/s41598-017-17292-3.

Luyten, J., J. Pedlosky, and H. Stommel, 1983: The ventilated thermocline. *J. Phys. Oceanogr.*, **13**, 292–309, https://doi.org/10.1175/1520-0485(1983)013<0292:TVT>2.0.CO;2.

Marshall, J., and T. Radko, 2003: Residual-mean solutions for the Antarctic Circumpolar Current and its associated overturning circulation. *J. Phys. Oceanogr.*, **33**, 2341–2354, https://doi.org/10.1175/1520-0485(2003)033<2341:RSFTAC>2.0.CO;2.

——, and K. Speer, 2012: Closure of the meridional overturning circulation through Southern Ocean upwelling. *Nat. Geosci.*, **5**, 171–180, https://doi.org/10.1038/ngeo1391.

——, R. G. Williams, and A. J. G. Nurser, 1993: Inferring the subduction rate and period over the North Atlantic. *J. Phys. Oceanogr.*, **23**, 1315–1329, https://doi.org/10.1175/1520-0485(1993)023<1315:ITSRAP>2.0.CO;2.

——, D. Jamous, and J. Nilsson, 1999: Reconciling thermodynamic and dynamic methods of computation of water-mass transformation rates. *Deep-Sea Res. I*, **46**, 545–572, https://doi.org/10.1016/S0967-0637(98)00082-X.

Mashayek, A., R. Ferrari, S. Merrifield, J. R. Ledwell, L. St Laurent, and A. N. Garabato, 2017: Topographic enhancement of vertical turbulent mixing in the Southern Ocean. *Nat. Commun.*, **8**, 14197, https://doi.org/10.1038/ncomms14197.

McCartney, M. S., 1977: Subantarctic Mode Water. *A Voyage of Discovery: George Deacon 70th Anniversary Volume*, M. V. Angel, Ed., Pergamon Press, 103–119.

——, and L. D. Talley, 1982: The Subpolar Mode Water of the North Atlantic Ocean. *J. Phys. Oceanogr.*, **12**, 1169–1188, https://doi.org/10.1175/1520-0485(1982)012<1169:TSMWOT>2.0.CO;2.

McDougall, T. J., 1987a: Neutral surfaces. *J. Phys. Oceanogr.*, **17**, 1950–1964, https://doi.org/10.1175/1520-0485(1987)017<1950:NS>2.0.CO;2.

——, 1987b: Thermobaricity, cabbeling, and water-mass conversion. *J. Geophys. Res.*, **92**, 5448–5464, https://doi.org/10.1029/JC092iC05p05448.

——, and P. M. Barker, 2011: Getting started with TEOS-10 and the Gibbs Seawater (GSW) Oceanographic Toolbox. SCOR/IAPSO WG127 Doc., 28 pp., http://www.teos-10.org/pubs/Getting_Started.pdf.

——, and O. A. Krzysik, 2015: Spiciness. *J. Mar. Res.*, **73**, 141–152, https://doi.org/10.1357/002224015816665589.

Meredith, M. P., and A. M. Hogg, 2006: Circumpolar response of Southern Ocean eddy activity to a change in the southern annular mode. *Geophys. Res. Lett.*, **33**, L16608, https://doi.org/10.1029/2006GL026499.

Morrison, A. K., and A. Hogg, 2013: On the relationship between Southern Ocean overturning and ACC transport. *J. Phys. Oceanogr.*, **43**, 140–148, https://doi.org/10.1175/JPO-D-12-057.1.

Naveira Garabato, A. C., K. L. Polzin, B. A. King, K. J. Heywood, and M. H. Visbeck, 2004: Widespread intense turbulent mixing in the Southern Ocean. *Science*, **303**, 210–213, https://doi.org/10.1126/science.1090929.

——, L. Jullion, D. P. Stevens, K. J. Heywood, and B. A. King, 2009: Variability of Subantarctic Mode Water and Antarctic Intermediate Water in the Drake Passage during the late-twentieth and early-twenty-first centuries. *J. Climate*, **22**, 3661–3688, https://doi.org/10.1175/2009JCLI2621.1.

——, R. Ferrari, and K. L. Polzin, 2011: Eddy stirring in the Southern Ocean. *J. Geophys. Res.*, **116**, C09019, https://doi.org/10.1029/2010JC006818.

Nowlin, W. D., and J. M. Klinck, 1986: The physics of the Antarctic Circumpolar Current. *Rev. Geophys.*, **24**, 469–491, https://doi.org/10.1029/RG024i003p00469.

Nurser, A. J. G., R. Marsh, and R. G. Williams, 1999: Diagnosing water mass formation from air–sea fluxes and surface mixing. *J. Phys. Oceanogr.*, **29**, 1468–1487, https://doi.org/10.1175/1520-0485(1999)029<1468:DWMFFA>2.0.CO;2.

Ollitrault, M., and J. P. Rannou, 2013: ANDRO: An Argo-based deep displacement dataset. *J. Atmos. Oceanic Technol.*, **30**, 759–788, https://doi.org/10.1175/JTECH-D-12-00073.1.

——, and A. Colin de Verdière, 2014: The ocean general circulation near 1000-m depth. *J. Phys. Oceanogr.*, **44**, 384–409, https://doi.org/10.1175/JPO-D-13-030.1.

Pellichero, V., J. B. Sallée, C. C. Chapman, and S. M. Downes, 2018: The southern ocean meridional overturning in the sea-ice sector is driven by freshwater fluxes. *Nat. Commun.*, **9**, 1789, https://doi.org/10.1038/s41467-018-04101-2.

Pemberton, P., J. Nilsson, M. Hieronymus, and H. E. M. Meier, 2015: Arctic Ocean water mass transformation in *S–T* coordinates. *J. Phys. Oceanogr.*, **45**, 1025–1050, https://doi.org/10.1175/JPO-D-14-0197.1.

Piola, A. R., and D. T. Georgi, 1982: Circumpolar properties of Antarctic Intermediate Water and Subantarctic Mode Water. *Deep-Sea Res.*, **29**, 687–711, https://doi.org/10.1016/0198-0149(82)90002-4.

Price, J. F., 2001: Subduction. *Ocean Circulation and Climate: A 21st Century Perspective*, G. Siedler et al., Eds., International Geophysics Series, Vol. 103, Academic Press, 357–371.

Rintoul, S. R., 2018: The global influence of localized dynamics in the Southern Ocean. *Nature*, **558**, 209–218, https://doi.org/10.1038/s41586-018-0182-3.

——, and A. C. Naveira Garabato, 2013: Dynamics of the southern ocean circulation. *Ocean Circulation and Climate: A 21st Century Perspective*, 2nd ed., G. Siedler et al., Eds., International Geophysics Series, Vol. 103, Academic Press, 471–492.

Roemmich, D., J. Church, J. Gilson, D. Monselesan, P. Sutton, and S. Wijffels, 2015: Unabated planetary warming and its ocean structure since 2006. *Nat. Climate Change*, **5**, 240–245, https://doi.org/10.1038/nclimate2513.

Saenko, O. A., A. Schmittner, and A. J. Weaver, 2002: On the role of wind-driven sea ice motion on ocean ventilation. *J. Phys. Oceanogr.*, **32**, 3376–3395, https://doi.org/10.1175/1520-0485(2002)032<3376:OTROWD>2.0.CO;2.

Sallée, J.-B., K. Speer, and R. Morrow, 2008: Response of the Antarctic Circumpolar Current to atmospheric variability. *J. Climate*, **21**, 3020–3039, https://doi.org/10.1175/2007JCLI1702.1.

——, ——, S. Rintoul, and S. Wijffels, 2010: Southern Ocean thermocline ventilation. *J. Phys. Oceanogr.*, **40**, 509–529, https://doi.org/10.1175/2009JPO4291.1.

Sloyan, B. M., and S. R. Rintoul, 2001: The Southern Ocean limb of the global deep overturning circulation. *J. Phys. Oceanogr.*, **31**, 143–173, https://doi.org/10.1175/1520-0485(2001)031<0143:TSOLOT>2.0.CO;2.

——, L. D. Talley, T. K. Chereskin, R. Fine, and J. Holte, 2010: Antarctic Intermediate Water and Subantarctic Mode Water formation in the southeast Pacific: The role of turbulent mixing. *J. Phys. Oceanogr.*, **40**, 1558–1574, https://doi.org/10.1175/2010JPO4114.1.

Speer, K., S. R. Rintoul, and B. Sloyan, 2000: The diabatic Deacon cell. *J. Phys. Oceanogr.*, **30**, 3212–3222, https://doi.org/10.1175/1520-0485(2000)030<3212:TDDC>2.0.CO;2.

Stommel, H., 1979: Determination of water mass properties of water pumped down from the Ekman layer to the geostrophic flow below. *Proc. Natl. Acad. Sci. USA*, **76**, 3051–3055, https://doi.org/10.1073/pnas.76.7.3051.

Talley, L. D., 1996: Antarctic Intermediate Water in the South Atlantic. *The South Atlantic: Present and Past Circulation*, Springer, 219–238, https://doi.org/10.1007/978-3-642-80353-6_11.

Tamsitt, V., R. P. Abernathey, M. R. Mazloff, J. Wang, and L. D. Talley, 2018: Transformation of deep water masses along Lagrangian upwelling pathways in the Southern Ocean. *J. Geophys. Res. Oceans*, **123**, 1994–2017, https://doi.org/10.1002/2017JC013409.

Walin, G., 1982: On the relation between sea-surface heat flow and thermal circulation in the ocean. *Tellus*, **34**, 187–195, https://doi.org/10.3402/tellusa.v34i2.10801.

Zika, J. D., B. M. Sloyan, and T. J. McDougall, 2009: Diagnosing the Southern Ocean overturning from tracer fields. *J. Phys. Oceanogr.*, **39**, 2926–2940, https://doi.org/10.1175/2009JPO4052.1.